Bio-Design and Manufacturing (2024) 7:670–686
https://doi.org/10.1007/s42242-024-00279-1

RESEARCH ARTICLE

Enhanced wear resistance, antibacterial performance, and biocompatibility using nanotubes containing nano-Ag and bioceramics in vitro

Qingge Wang[1] · Jia Liu[2] · Hong Wu[1] · Jingbo Liu[1] · Yaojia Ren[1] · Luxin Liang[3] · Xinxin Yan[4] · Ian Baker[5] · Shifeng Liu[6] · V. V. Uglov[7] · Chengliang Yang[2] · Liqiang Wang[8]

Received: 3 July 2023 / Accepted: 2 April 2024 / Published online: 11 July 2024

Abstract

A good Ti-based joint implant should prevent stress shielding and achieve good bioactivity and anti-infection performance. To meet these requirements, the low-elastic-modulus alloy—Ti–35Nb–2Ta–3Zr—was used as the substrate, and functional coatings that contained bioceramics and Ag ions were prepared for coating on TiO_2 nanotubes (diameter: (80±20) nm and (150±40) nm) using anodization, deposition, and spin-coating methods. The effects of the bioceramics (nano-β-tricalcium phosphate, microhydroxyapatite (micro-HA), and meso-$CaSiO_3$) and Ag nanoparticles (size: (50±20) nm) on the antibacterial activity and the tribocorrosion, corrosion, and early in vitro osteogenic behaviors of the nanotubes were investigated. The tribocorrosion and corrosion results showed that the wear rate and corrosive rate were highly dependent on the features of the nanotube surface. Micro-HA showed great wear resistance with a wear rate of $(1.26\pm0.06)\times10^{-3}$ $mm^3/(N\cdot m)$ due to adhesive and abrasive wear. Meso-$CaSiO_3$ showed enhanced cell adhesion, proliferation, and alkaline phosphatase activity. The coatings that contained nano-Ag exhibited good antibacterial activity with an antibacterial rate of ≥89.5% against *Escherichia coli*. These findings indicate that hybrid coatings may have the potential to accelerate osteogenesis.

Qingge Wang and Jia Liu have contributed equally to this work.

✉ Hong Wu
hwucsu@csu.edu.cn; wuhong927@126.com

✉ Chengliang Yang
stbyyl@126.com

✉ Liqiang Wang
wang_liqiang@sjtu.edu.cn

1 State Key Laboratory of Powder Metallurgy, Central South University, Changsha 410083, China

2 Affiliated Hospital of Youjiang Medical University for Nationalities, Guangxi Key Laboratory for Preclinical and Translational Research on Bone and Joint Degenerative Diseases, Guangxi Zhuang Autonomous Region Engineering Research Center for Biomaterials in Bone and Joint Degenerative Diseases, Guangxi Key Laboratory for Biomedical Material Research, Baise 533000, China

3 Department of Orthopedics, The Second Xiangya Hospital, Central South University, Changsha 410011, China

4 Department of Orthopedics, Renmin Hospital, Wuhan University, Wuhan 430060, China

5 Thayer School of Engineering, Dartmouth College, Hanover, NH 03755-8000, USA

6 School of Metallurgical Engineering, Xi'an University of Architecture and Technology, Xi'an 710055, China

7 Belarusian State University, 220030 Minsk, Belarus

8 State Key Laboratory of Metal Matrix Composites, School of Material Science and Engineering, Shanghai Jiao Tong University, Shanghai 200240, China

Graphic abstract

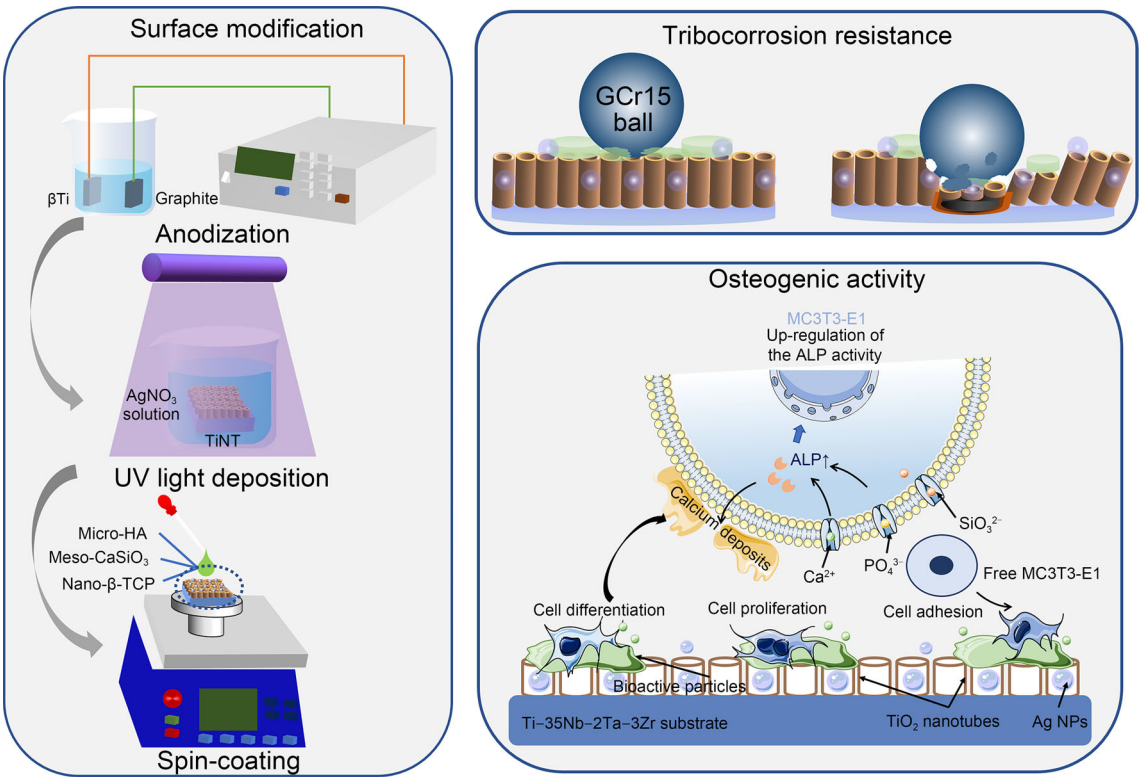

Keywords βTi alloy · Surface modification · Wear resistance · Corrosion resistance · Osteogenic behavior · Antibacterial activity

Introduction

Millions of knee and hip replacement surgeries are performed every year globally because of joint injuries and aging [1]. Titanium alloys have been used in the biomedical field for half a century owing to their high strength, low density, and outstanding biocompatibility [2–5]. However, a mismatch in the elastic modulus between titanium joint and bone (about 100 GPa vs. 15–30 GPa) leads to stress shielding, which can result in bone resorption and implant failure. To prevent this outcome, novel β and near-β-type Ti-based alloys with a low elastic modulus (30–60 GPa) close to that of human bone have been developed [6–11]. A specimen of the alloy—Ti–35Nb–2Ta–3Zr—which is referred to as TNTZ, having an elastic modulus of 48 GPa, was developed for this purpose [12–14]. TNTZ was implanted into the iliac crests of goats, and after three weeks, it was found to have improved both load transduction and bone remodeling [15]. In another study, Zn nanoparticles (NPs) were incorporated into a TNTZ alloy via friction stir processing, achieving the up-regulated expression of adhesion and antibacterial properties (antibacterial rate: 83%) [16]. In addition, TiO_2 NPs incorporated into a TNTZ substrate improved corrosion resistance in Hank's solution [17]. The above-discussed studies indicate that after modification, TNTZ exhibited good corrosion resistance, antibacterial ability, and osseointegration. Nevertheless, the bioactivity and wear resistance of TNTZ need to be further improved.

Surface modification is a strategy commonly used to increase the bioactivity and wear resistance of titanium alloys [18–22]. Anodization is a surface modification technology that can introduce ordered TiO_2 nanotubes (TNTs) onto the surfaces of titanium alloys by adjusting the parameters of oxidation duration, oxidation voltage, electrolyte solution type, and concentration [23]. Yu et al. reported that when the diameter of the nanotubes was adjusted, larger TNTs improved osteogenic differentiation [24]. Interestingly, Alves et al. reported that TNTs enriched with Ca and P exhibited improved osteoblastic functions [25]. Meanwhile, Zhang et al. developed TNT coatings codoped with Sr and Ca that promoted cell proliferation and osteogenic activities [26]. Furthermore, Shen et al. produced dexamethasone-doped TNTs covered with chitosan multilayer films that showed good osteogenic behavior [27]. Most of these studies

focused on osteogenic ability, but did not consider antibacterial properties.

Ag is a stable antibacterial agent that can be incorporated in Ti alloys in many studies. Several studies have investigated the antibacterial mechanisms of Ag NPs. Ag NPs promoted bacteria to generate reactive oxygen species, which eventually killed the bacteria [28]. Controlling the Ag concentration is key to achieving good antibacterial effects with low cytotoxicity. It has been reported that the antibacterial effect and cell activity of Ti–6Al–4 V/Ag produced via friction stir processing reached a balance when the Ag content was 4.3%–5.6% (mass fraction) [29]. However, Ag displayed obvious cytotoxicity when the Ag concentration was greater than 0.7 mg/L [30, 31]. Thus, it is necessary to control the Ag ion release by designing a slow release layer with bioactivity.

Bioceramics act as a slow ion release platform and can benefit osteogenic behavior. It was reported that hydroxyapatite (HA) layers containing Ag ions in a porous TiO_2 coating provided continuous Ag ion release [32]. These layers showed good cell viability and had a positive effect on the formation of bone-like calcium sulfate. Similarly, chitosan-embedded calcium silicate ($CaSiO_3$) layers were used as a drug release carrier that had good biocompatibility, osteoconductivity, and degradability [33]. Similarly, β-tricalcium phosphate (β-TCP) coatings loaded with Zn, Mg, and Ti ions were shown to accelerate bone healing [34]. However, the interaction between Ag ion release and these three bioceramics has not been clarified. After these bioceramics were coated onto the TNTs, their biological performance was investigated. Generally, hip implants involve the in vivo interaction of mechanical wear and static corrosion [1]. Thus, it is necessary to evaluate tribocorrosion performance.

In this study, HA, $CaSiO_3$, and β-TCP having different particle sizes were coated onto TNTs loaded with Ag NPs. The wear behavior in simulated body fluid (SBF) and the electrochemical behavior of the coatings were investigated. In addition, in vitro studies were conducted to identify the osteogenic capacity (preosteoblast adhesion, proliferation, and alkaline phosphatase (ALP) activity) and antibacterial properties of the coatings.

Materials and methods

Materials

The Ti–35Nb–2Ta–3Zr alloy (mass ratio) was produced by mixing high-purity Ti sponge, Ti–Nb interalloy, high-purity Ta, and high-purity Zr in a vacuum arc melting furnace. The ingot was remelted three times under an argon atmosphere and then annealed for homogenization in vacuum at 950 °C for 1 h. TNTZ plates (referred to as βTi) measuring 10 mm×10 mm×1 mm were polished with 80, 400, 600, 1000, 1500, 2000, and 3000 grit sandpapers and were then cleaned with deionized water and ethanol. TNTs were deposited on the βTi substrates using a commercial anodization device (62024P-600–8, Chroma, USA) for 30 min at 30 V direct current (DC) in a 0.1 mol/L HF aqueous solution. The TNTs were then annealed for 2 h at 450 °C [35] (referred to as TiNT). The TiNT was soaked in a 0.1 mol/L $AgNO_3$ aqueous solution for 10 min under ultraviolet (UV) radiation (365 nm wavelength) to incorporate the Ag NPs (referred to as TiNTAg). Micro-HA particles ((50.2±15.4) μm), meso-$CaSiO_3$ particles ((160.0±33.3) μm), and nano-β-TCP particles ((310±90) nm), each at a concentration of 1 mg/mL polyethylene glycol solution, were applied to the TiNTAg via spin coating at a speed of 3000 r/min for 20 s (referred to as TiNTAg@HA, TiNTAg@$CaSiO_3$, and TiNTAg@β-TCP, respectively) [31]. Then, the specimens were dried in an oven. The hybrid coating process is shown in Fig. 1a. The sizes of the HA, $CaSiO_3$, and β-TCP particles were characterized using a scanning electron microscope (SEM) (see Fig. S1 in Supplementary Information).

Microstructural characterization

The phase analysis and microstructural characterization of the specimens were performed via X-ray diffraction (XRD) using Cu-Kα radiation at 40 kV and 40 mA with a step size of 0.02 (°)/s (D8 ADVANCE, Bruker, Germany) as well as using a field electron gun SEM at 5–20 kV (250 FEG, Quanta, USA). The location of Ag in the TNTs was characterized via high-resolution transmission electron microscopy (HRTEM) and selected area electron diffraction (SAED) using an FEI Tecnai G2F20 operated at 200 kV. Fourier transform infrared spectroscopy (FTIR, Nicolet iS50, Thermo, USA) was conducted on TiNTAg@HA, TiNTAg@$CaSiO_3$, and TiNTAg@β-TCP over the wavenumber range of 500–4000 cm^{-1}. To evaluate the bonding force between the coatings and the substrate, scratch tests were performed, which are presented in Supplementary Information.

Ag ion release

The specimens were deposited into an SBF solution at 37 °C for various durations (6 h, 12 h, 1 d, 2 d, 3 d, 5 d, 7 d, and 14 d), and the resulting ion release was measured using a plasma spectrometer (SPECTRO BLUE, Germany).

Tribocorrosion tests

Tribocorrosion tests were performed using an HT-1000 tribometer. The counterpart was a GCr15 steel ball with a 4-mm diameter [31]. The specimens were placed in a container filled with SBF solution. Tests were performed at a 4.9-N load

for 1800 s, with a circular motion of 4-mm sliding diameter and 4-Hz frequency. Then, the specimens were dried, and the three-dimensional (3D) structures of the surfaces were characterized using a super deep scene 3D microscope.

Corrosion tests

Electrochemical measurements of the specimens were taken by placing an SBF solution on a CS310OH electrochemical workstation with a three-electrode electrochemical cell, saturated calomel electrode, reference electrode, and a Pt foil electrode. When the open-circuit potential of the specimens reached a steady state, electrochemical impedance spectroscopy (EIS) was performed at frequencies of 10^{-2}–10^{5} Hz at room temperature. The resulting data were analyzed using View 3.1 software. Potentiodynamic polarization curves were obtained at a sweep rate of 1 mV/s.

In vitro experiments

Cell culture

MC3T3-E1 cells (mouse embryo osteoblast precursor cells from China Infrastructure of Cell Line Sources) were incubated in an a-minimum essential medium (a-MEM) (Gbico, Invitrogen, Inc., USA) containing 10% fetal bovine serum (Gibco, USA) and 1% penicillin/streptomycin (Life Technologies, USA) in an incubator (5% CO_2, 100% humidity, and 37 °C). The culture medium was replenished every two days.

Cell morphology

MC3T3-E1 cells were seeded onto the surfaces of each specimen at a density of 5×10^4 cells/well. After they had been incubated for 8 and 24 h, respectively, the MC3T3-E1 cells were cleaned three times and fixed with 2.5% glutaraldehyde (Sigma, USA) for 12 h. Subsequently, the cells were dehydrated with graded alcohol at concentrations of 30%, 50%, 70%, 80%, 90%, 95%, and 100% (volume fraction), and then were dehydrated with graded tertiary butanol solution at concentrations of 25%, 50%, 75%, and 100% (volume fraction), each for 5 min. The specimens were covered with gold before SEM observation.

Viability and cell proliferation of MC3T3-E1 cells

To assess the activity and proliferation of MC3T3-E1 cells, the cells were seeded onto the surfaces of the specimens at a density of 2×10^4 cells/well. The viability of MC3T3-E1 cells was measured quantitatively using the cell counting kit-8 (CCK-8, Dojindo, Japan) assay on Days 1, 3, and 5. The culture medium was removed. A solution containing 10% CCK-8 solution and 90% culture medium was added to each well and incubated at 37 °C for 30 min. The optical density of each well was measured using a microplate reader (PerkinElmer, USA) at 450 nm. The proliferation of the MC3T3-E1 cells was qualitatively evaluated using live cell staining on Days 1, 3, and 5. The specimens were immersed in 2 μmol/L calcein–AM (Dojindo, Japan) for live cells for 30 min at 37 °C, and live cells (green) on the surfaces of the specimens were recorded with a fluorescence microscope (Leica, Germany).

Alkaline phosphatase activity

MC3T3-E1 cells were introduced onto the surfaces of the specimens at a cell density of 2×10^4 cells/well for seven days to evaluate the ALP activity. For quantitative testing, a radio immunoprecipitation assay (RIPA) lysis buffer (Beyotime, China) was placed in each well and reacted for 15 min. Afterward, the lysed solutions were centrifuged at 12,000 r/min for 10 min and then measured using an ALP testing kit (Beyotime, China) and a microplate reader at 410 nm (PerkinElmer, USA). The ALP activity was standardized using the total protein content determined by a bicinchoninic acid (BCA) assay kit (Beyotime, China) using a microplate reader at 570 nm.

Antibacterial activity

Escherichia coli (*E. coli*) (ATCC25922) was used to evaluate the antibacterial activity of the specimens. For the qualitative tests, the inhibition ring against *E. coli* was used to assess antibacterial ability. Bacterial broth (100 μL) at a concentration of 1×10^7 CFU/mL (CFU: colony-forming units) was added to the plates containing Luria–Bertani (LB) solid medium. Then, the specimens were incubated for 12 h. For the quantitative tests, 1 mL bacterial broth having a concentration of 1×10^7 CFU/mL was seeded into each well of the surfaces of specimens in 24-well plates and cultured for 12 h. The bacteria were separated from the specimen into 10 mL of diluted phosphate-buffered saline (PBS) using ultrasonic disruption for 5 min. Bacterial broth (100 μL) at a concentration of 2000 CFU/mL was added onto LB solid medium for each group. The bacterial broth was spread evenly on the plates using a sterilized spatula and then placed in an incubator for 12 h. The antibacterial rate was calculated using the following formula:

$$\text{Antibacterial rate} = (1 - N_x/N_b) \times 100\%,$$

where N_x and N_b are the number of colonies on a solid medium for each group.

Statistical analysis

All the experiments were performed in quadruplicate. The results were presented as the mean±standard deviation. The statistical significance was analyzed using a one-way analysis of variance (ANOVA). Notable differences between the specimens were indicated as follows: $^{*}p<0.05$, $^{**}p<0.01$, and $^{***}p<0.001$.

Results

Surface characterization

Figure 1b shows the secondary electron (SE) image of the specimens with two different TNT diameters ((80±20) nm and (150±40) nm) of homogeneously distributed TNTs. Figure 1c shows that the Ag element exists at the yellow location, and the TiNTAg detail is shown in Fig. S2 (Supplementary Information). Figures 1d–1f show the specimens with HA, $CaSiO_3$, and β-TCP coated onto the TNTs and Ag NPs via spin coating. Figure 2a shows the phase present in the specimens. Typical peaks for both anatase (25.28°, 38.58°, 48.05°) and βTi (38.48°, 55.54°, 69.61°) are present after annealing, which indicates that the TNTs were transformed from the amorphous state into anatase. No peaks for the Ag NPs were present in the TiNTAg pattern due to the small size and low volume fraction of Ag particles. Peaks of HA (28.94°; 35.47°; 42.13°; 57.13°), $CaSiO_3$ (27.69°; 42.12°; 46.03°), and β-TCP (37.14°; 46.74°; 52.94°) were present in the patterns for TiNTAg@HA, TiNTAg@$CaSiO_3$, and TiNTAg@β-TCP, respectively, indicating that the bioactive coating was successfully coated onto the nanotubes.

The bond structure and functional groups in TiNTAg@HA, TiNTAg@$CaSiO_3$, and TiNTAg@β-TCP (Fig. 2b) were investigated via FTIR spectroscopy. The troughs corresponding to the bonding of the CO_3^{2-} and H_2O groups are present in the spectra of all the three specimens at 1540, 1630, and 3386 cm^{-1}. The presence of the characteristic bands of CO_3^{2-} indicates that C is dissolved in polyethylene glycol as well as in the HA, $CaSiO_3$, and β-TCP crystals [32]. The strong bands in the TiNTAg@HA spectra at 602 and 1033 cm^{-1} correspond to the bending and asymmetric stretching modes of the PO_4^{3-} groups, respectively. The band at 1033 cm^{-1} in the TiNTAg@HA spectra arises from O–P–O [36]. The bands at 934, 1008, and 1062 cm^{-1} correspond to the different bending modes of SiO_3^{2-}. In the TiNTAg@β-TCP spectra, the bands at 573, 601, and 1019 cm^{-1} correspond to PO_4^{3-} [37]. These results show that HA, $CaSiO_3$, and β-TCP particles were successfully coated onto TiNTAg.

Figure 2c shows the Ag^+ concentration of the specimens as a function of time. The Ag^+ concentration was as high as 0.85 mg/L in the TiNTAg group. The cumulative Ag^+ concentrations were 0.54, 0.33, and 0.61 mg/L in TiNTAg@HA, TiNTAg@$CaSiO_3$, and TiNTAg@β-TCP, respectively, suggesting that the slow release of the Ag^+ was achieved by covering the bioceramics. The total Ag^+ release was dominated by the dissolution of TiNTAg.

To determine the spatial distribution of the Ag NPs in the TNTs, TiNTAg was characterized using a transmission electron microscopy (TEM) (Figs. 1g–1j). As expected, the Ag NPs, which were (50±20) nm in diameter, were present inside the TNTs (Figs. 1g and 1h). To identify the exact locations of the Ag NPs, HRTEM imaging and SAED were obtained, as shown in Figs. 1i and 1j. The crystalline structure of Ag inside the TNTs is evident in Fig. 1j, and an interplanar distance d_{hkl} (111) of 0.2359 nm was measured. Based on these results, it was confirmed that the Ag NPs were in the metallic state and were embedded into the nanotubes.

Tribocorrosion behavior

The wear interactions between a joint implant and the surrounding tissue are crucial to the lifetime of the implant. According to the American Society of Testing Materials (ASTM) F3446-20, joint implants need to meet the requirements of wear and friction. Figure 3a shows the coefficient of friction (COF) for βTi, TiNT, TiNTAg, TiNTAg@HA, TiNTAg@$CaSiO_3$, and TiNTAg@β-TCP under tribocorrosion conditions for 1800 s. For the substrate, the COF was 0.61. Initially, the COF of the TiNT was considerably lower than 0.61; however, after a short period, the COF increased and remained stable at 0.75. The COFs of TiNTAg@HA, TiNTAg@$CaSiO_3$, and TiNTAg@β-TCP were low and stable for 600 s because of the bioceramics.

The wear rate ($mm^3/(N{\cdot}m)$) was calculated based on the measurements of the wear tracks discussed in [38]:

$$\text{wear rate} = V/(W \cdot L) = S \cdot C/(W \cdot 2\pi r \cdot n), \tag{1}$$

where V is the volume loss, W is the normal load, L is the sliding distance, S is the cross-sectional area of the worn surface, C is the sliding girth, r is the sliding radius, and n is the number of wear circles. The cross-sectional profiles of the wear tracks are shown in Fig. 3b. The wear tracks of βTi and TiNTAg@$CaSiO_3$ were the deepest and had a maximum depth of about 90 μm, whereas TiNTAg@HA had the shallowest tracks, which were about 60 μm. As shown in Fig. 3c, the wear rates of βTi, TiNT, TiNTAg, TiNTAg@HA, TiNTAg@$CaSiO_3$, and TiNTAg@β-TCP in the SBF solution are $(2.03\pm0.24)\times10^{-3}$, $(1.62\pm0.01)\times10^{-3}$, $(1.53\pm0.13)\times10^{-3}$, $(1.26\pm0.06)\times10^{-3}$, $(1.86\pm0.11)\times10^{-3}$, and $(1.62\pm0.03)\times10^{-3}$ $mm^3/(N{\cdot}m)$, respectively. Notably, the TiNTAg@HA shows the lowest wear rate,

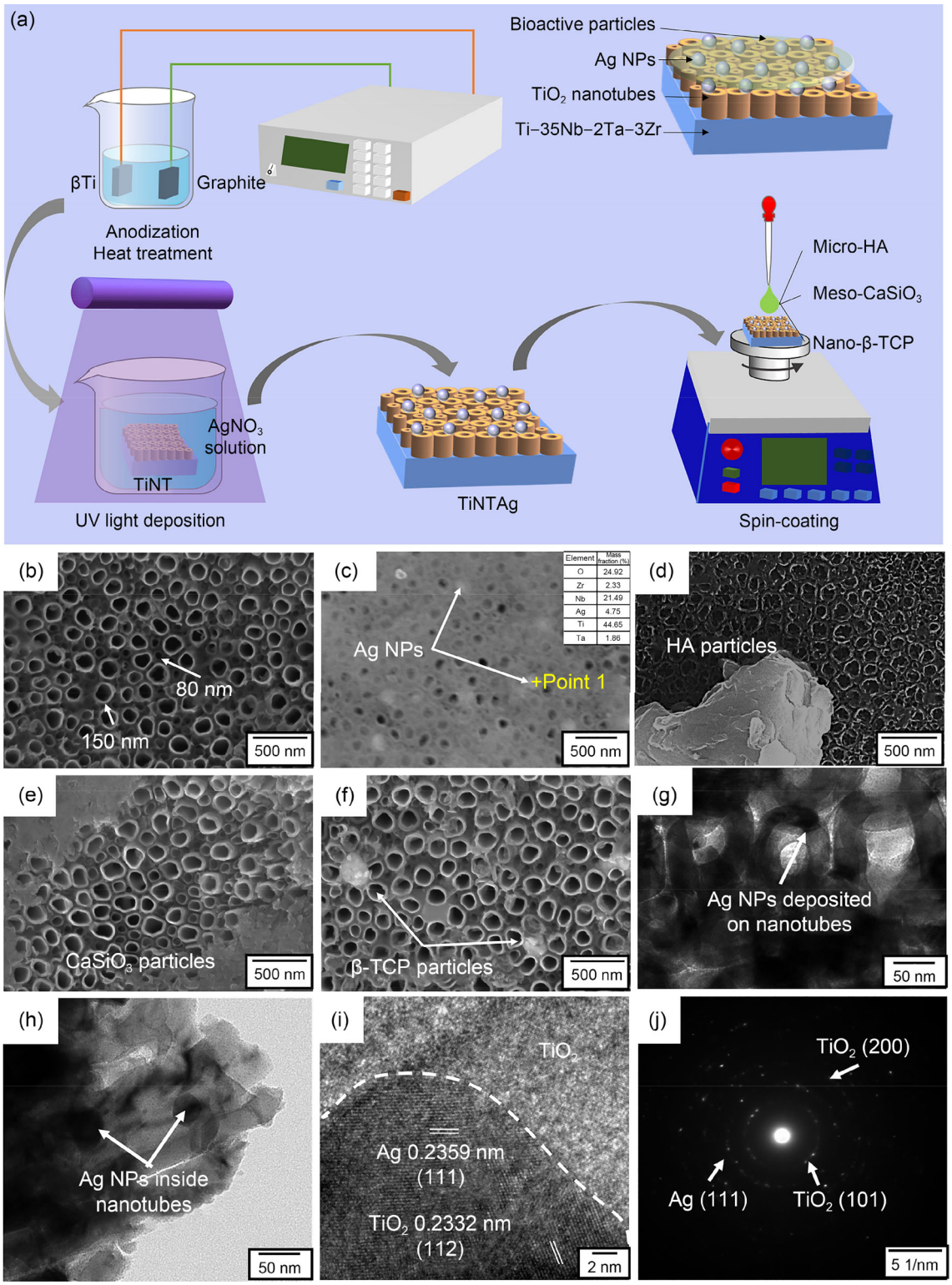

Fig. 1 **a** Schematic of the hybrid coating preparation process; SE images of **b** TiNT, **c** TiNTAg, **d** TiNTAg@HA, **e** TiNTAg@$CaSiO_3$, and **f** TiNTAg@β-TCP; **g** BF TEM image of TiNTAg viewed perpendicular to the surface; **h** BF TEM image showing the location of Ag NPs within the TNTs; **i** HRTEM image of Ag NPs in (**h**); **j** SAED pattern of Ag NP in (**h**). SE: secondary electron; BF: bright field; TEM: transmission electron microscopy; NPs: nanoparticles; HRTEM: high-resolution transmission electron microscopy; SAED: selected area electron diffraction; UV: ultraviolet

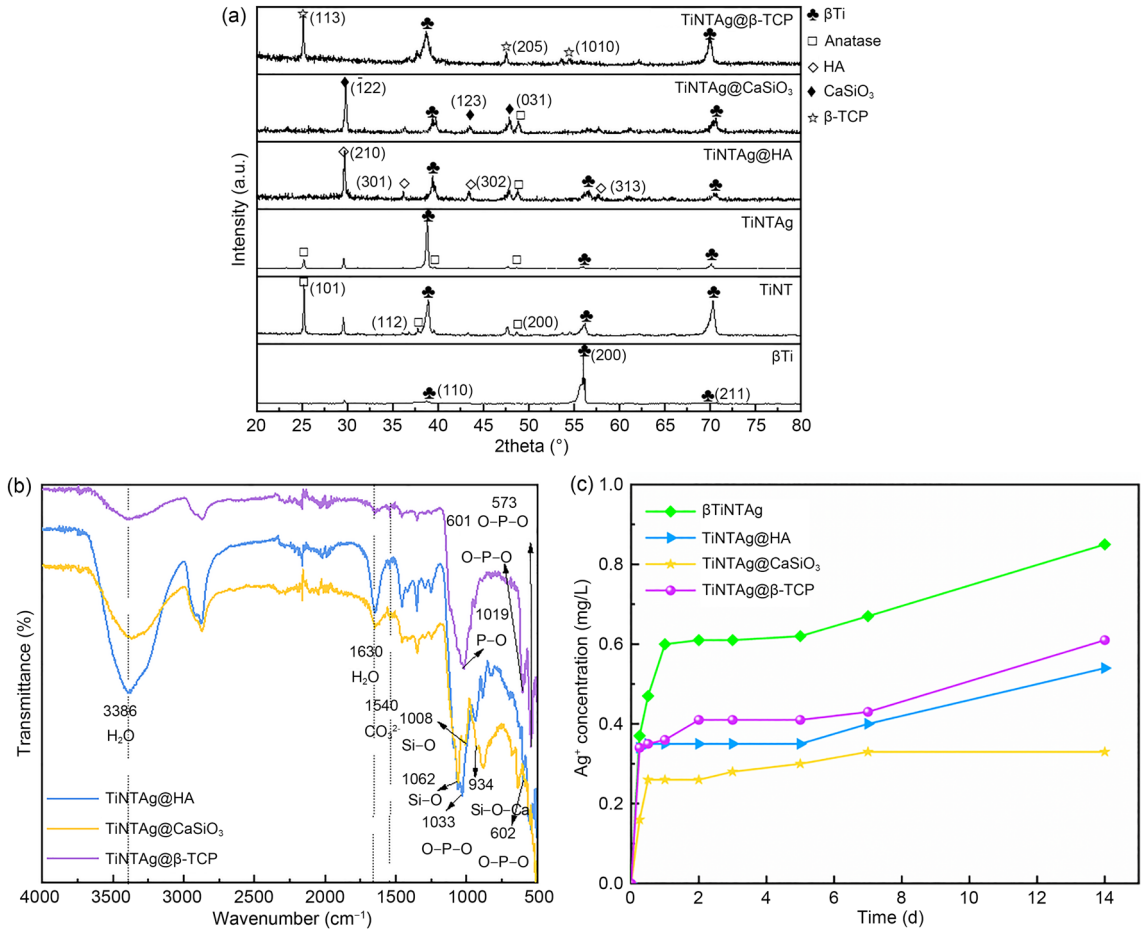

Fig. 2 **a** XRD patterns of the specimens; **b** FTIR spectra of TiNTAg@HA, TiNTAg@$CaSiO_3$, and TiNTAg@β-TCP; **c** Ag^+ release vs. time after immersion in the SBF solution. XRD: X-ray diffraction; FTIR: Fourier transform infrared spectroscopy; SBF: simulated body fluid

which is also indicated by the 3D surface morphologies (Figs. 3d–3i).

Figure 4 shows the SE images of the surfaces after the tribocorrosion tests. The wear track surface of the βTi is quite wide, and microplowing can be clearly observed (Figs. 4a and 4b), accompanied by considerable plastic deformation. The wear tracks of the other specimens were shallow, and the wear debris consisted of spalled coatings and oxide particles. In particular, TiNTAg@HA showed the narrowest wear track. The wear mechanism is discussed in "Wear behavior" section.

Corrosion behavior

Figure 5 shows the electrochemical characteristics of all the specimens in the SBF solution. To determine the corrosion process, the potentiodynamic polarization curves of βTi, TiNT, TiNTAg, TiNTAg@HA, TiNTAg@$CaSiO_3$, and TiNTAg@β-TCP are presented in Fig. 5a.

E_{corr} and i_{corr} were obtained through Tafel extrapolation (see Table 1). E_{corr} represents the potential difference between metal surface and corrosion medium. Generally, the more positive the E_{corr} value, the greater the corrosion resistance. TiNTAg@β-TCP showed a more positive E_{corr} compared to the other specimens. i_{corr} is related to the corrosion rate (CR) and mass loss rate (MR). The calculation is presented in Supplementary Information. The lower the i_{corr} value, the greater the corrosion resistance. TiNTAg@β-TCP showed the lowest i_{corr} of 0.001 mA.

Consequently, βTi showed the highest MR and CR (12.54 g/(m^2·d) and 0.73 mm/a, respectively), whereas the MR and CR of TiNTAg@β-TCP were only 0.26 g/(m^2·d) and 0.02 mm/a, respectively.

Figure 5b shows the Nyquist plots of the EIS spectra of the specimens. Table 2 lists the EIS fitting parameters of the specimens. The corrosion resistance improves with the increase in the arc radius of the Nyquist plots. The arc radius values were ranked as βTi < TiNTAg@$CaSiO_3$ < TiNTAg@HA < TiNT < TiNTAg < TiNTAg@β-TCP. Alternating current (AC) impedance at high frequencies showed the coating characteristics, whereas AC impedance at low frequencies

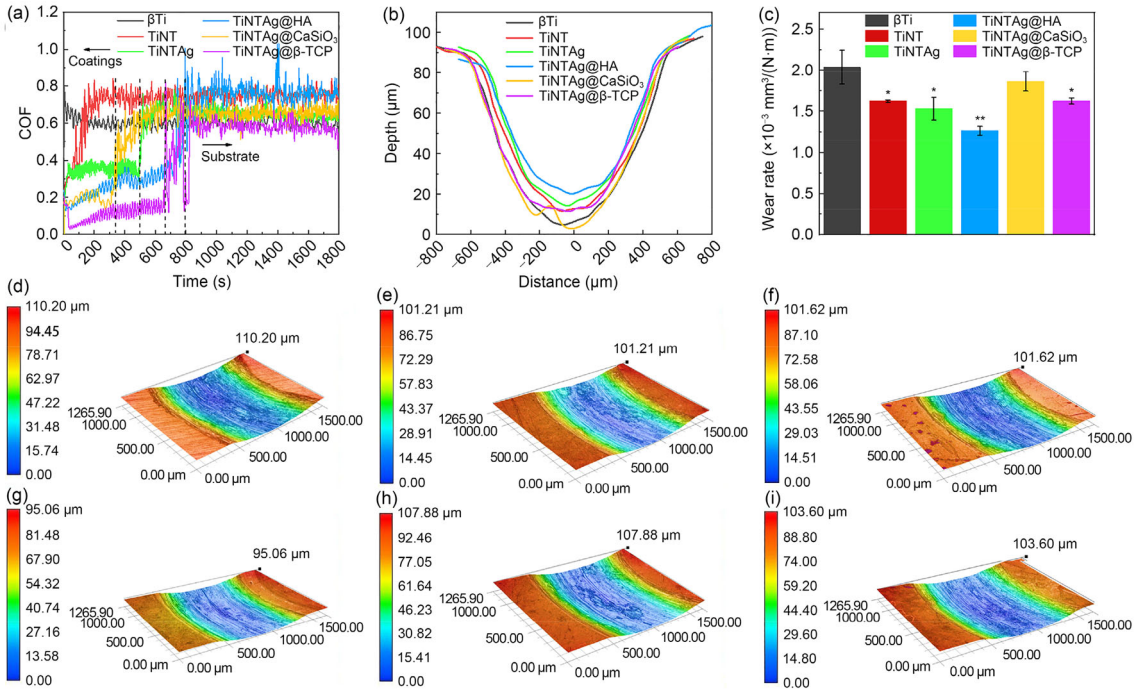

Fig. 3 **a** COFs of specimens in the SBF solution at (37±0.5) °C under tribocorrosion (the dashed lines represent the failure point of different coatings during the friction process); **b** cross-sectional profiles of the wear tracks for each specimen; **c** wear rate under tribocorrosion conditions; three-dimensional surface morphologies recorded after tribocorrosion tests for **d** βTi, **e** TiNT, **f** TiNTAg, **g** TiNTAg@HA, **h** TiNTAg@$CaSiO_3$, and **i** TiNTAg@β-TCP. Data are represented as mean±standard deviation (n=3); $^{*}p<0.05$ and $^{**}p<0.01$ compared to the βTi group. COF: coefficient of friction; SBF: simulated body fluid

reflected the double-layer capacitance (C_{dl}) and charge transfer resistance (R_{ct}) [39]. The Bode plots and phase angle plots in Figs. 5c and 5d demonstrate that TiNTAg@β-TCP exhibits a higher |Z| and higher phase angle with greater stability of the corrosion product passive film, and |Z| and phase angle are much higher than those of βTi. In summary, the TiNTAg@β-TCP coating considerably increased corrosion protection.

The equivalent electric circuit (EEC) is shown in Fig. 5e, where the upper part represents the equivalent circuit of the βTi and the lower part reflects the equivalent circuit of TiNT, TiNTAg, TiNTAg@HA, TiNTAg@$CaSiO_3$, and TiNTAg@β-TCP. R_s, R_f, CPE, and R_{ct} are the solution resistance, oxide film resistance, constant phase element, and charge transfer resistance, respectively.

Effect of coatings on the MC3T3-E1 cells

Adhesion, viability, and proliferation of the MC3T3-E1 cells

Figure 6 shows the osteoblast shapes after 8 and 24 h of incubation. Specifically, cells having a spindle shape adhered to the βTi surface. However, the number of MC3T3-E1 cells was substantially lower on the TiNTAg surface than on the βTi surface due to the toxicity of the Ag NPs, which can lead to oxidative stress [40]. A large number of cells on the surfaces of TiNTAg@HA, TiNTAg@$CaSiO_3$, and TiNTAg@β-TCP had polygonal osteoblast shapes and spread over a considerably greater area than those on the surface of the βTi, which showed high cell adhesion.

Figure 7 shows the fluorescent staining images and the viability of MC3T3-E1 cells after 1, 3, and 5 days. For βTi, TiNT, TiNTAg@HA, TiNTAg@$CaSiO_3$, and TiNTAg@β-TCP, the live cells cultured for 3 and 5 days exhibited remarkable increase in OD value, which indicated great cell proliferation ability. The large number of cells on TiNTAg@HA, TiNTAg@$CaSiO_3$, and TiNTAg@β-TCP exhibited considerably higher proliferative capacity compared to those on βTi. As shown in Fig. 7b, TiNTAg exhibited obvious toxicity due to a significant negative difference in OD value compared to βTi. TiNTAg@HA, TiNTAg@$CaSiO_3$, and TiNTAg@β-TCP exhibited cell viability as good as the βTi. This shows that the addition of bioceramics reduces the toxicity of Ag.

Alkaline phosphatase activity of MC3T3-E1 cells

Figure 8 shows the quantitative results of the ALP activity of MC3T3-E1 cells. The ALP activity of the specimens follows the trend: TiNTAg@$CaSiO_3$ > TiNTAg@HA > TiNTAg@β-TCP > TiNT > βTi > TiNTAg. Compared to βTi, all the

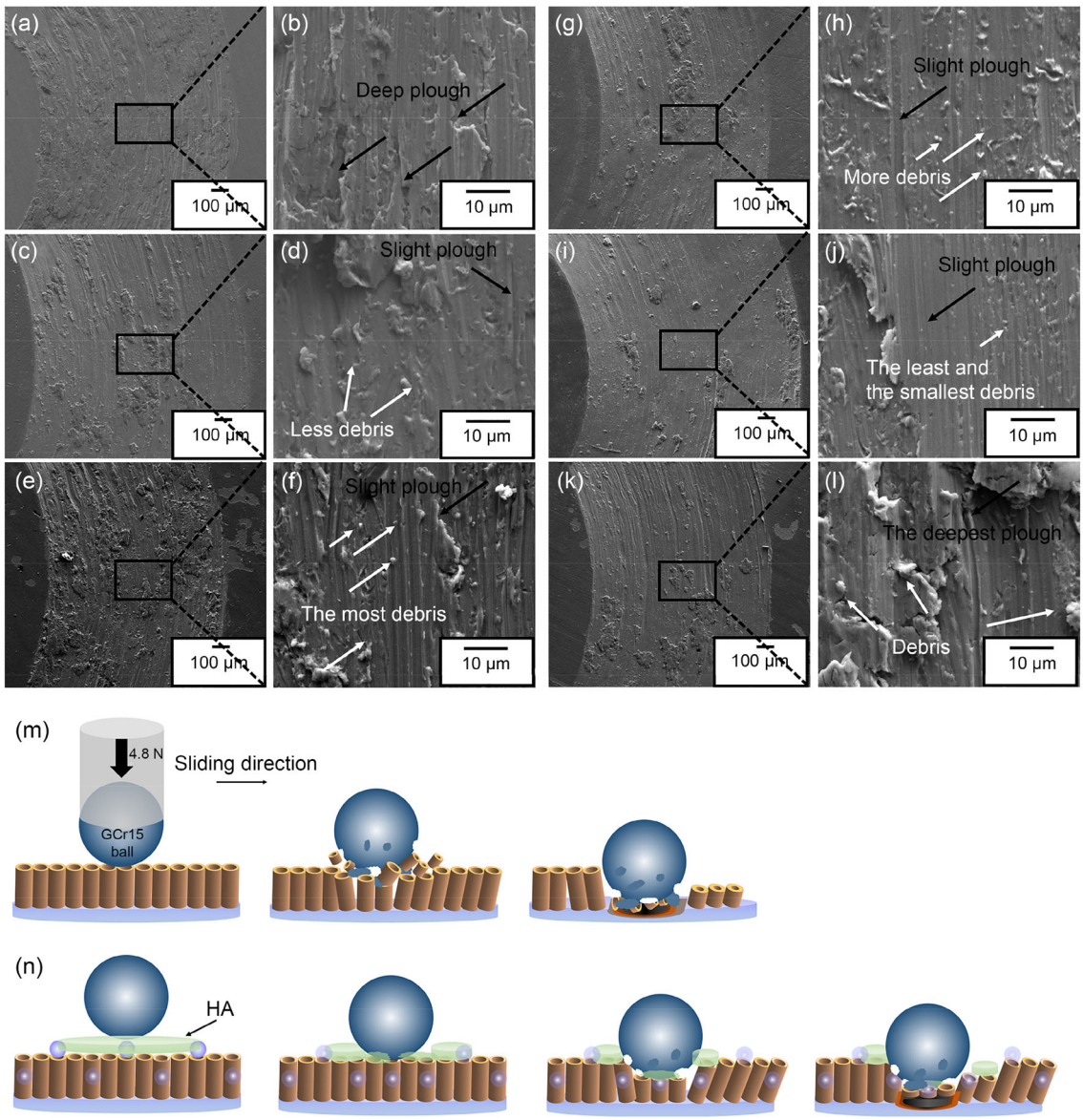

Fig. 4 SE images of the wear tracks after tribocorrosion tests in the SBF solution for **a**, **b** βTi, **c**, **d** TiNT, **e**, **f** TiNTAg, **g**, **h** TiNTAg@HA, **i**, **j** TiNTAg@$CaSiO_3$, and **k**, **l** TiNTAg@β-TCP. Schematic of the tribocorrosion process of **m** TiNT and **n** TiNTAg@HA in the SBF solution. SE: secondary electron; SBF: simulated body fluid

specimens show improvement in terms of ALP activity, except for TiNTAg. TiNTAg@$CaSiO_3$ improves osteogenesis in vitro by considerably promoting ALP activity.

Antibacterial activity

Figure 9 shows the antibacterial results of the inhibition ring experiment against *E. coli*. These results indicate that the βTi and TiNT groups have no antibacterial effect. It is worth noting that the groups containing Ag show excellent antibacterial activity. The antibacterial rates of TiNTAg, TiNTAg@HA, TiNTAg@$CaSiO_3$, and TiNTAg@β-TCP are 94.7%, 90.7%, 89.5%, and 92.8%, respectively. These results show that Ag NPs exhibit efficient antibacterial behavior. The antibacterial mechanisms of the Ag NPs were outlined in our previous study [31].

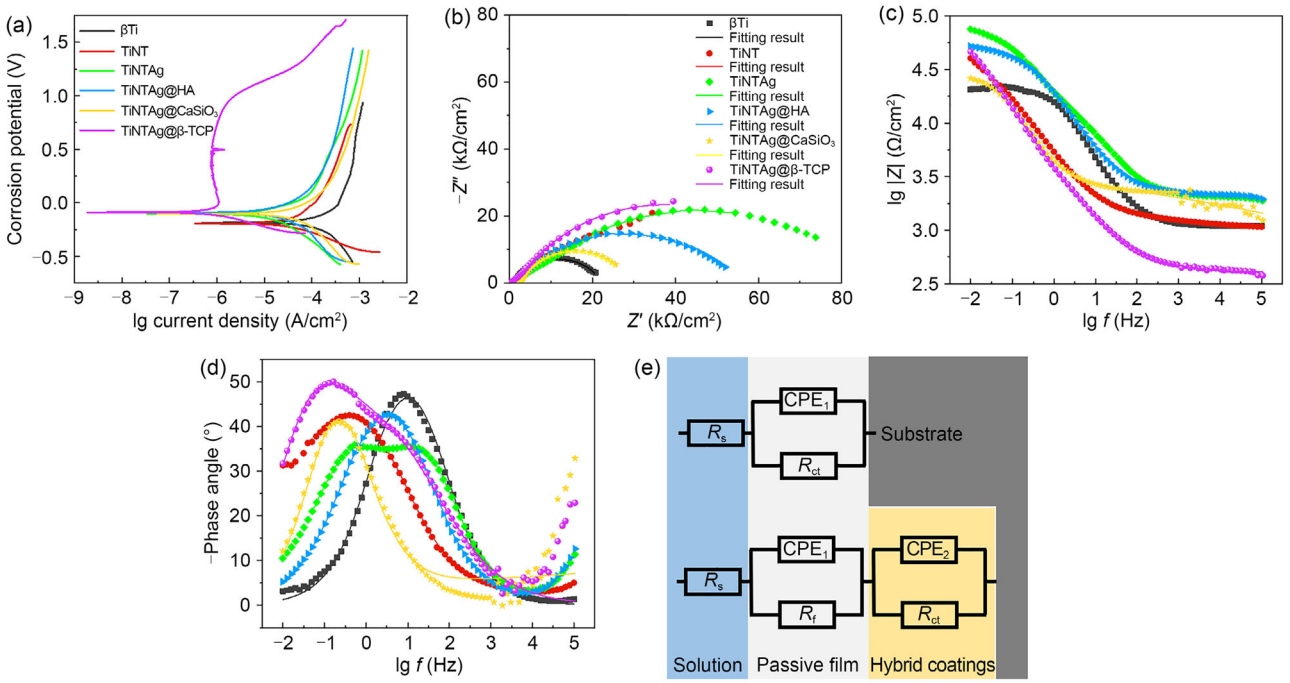

Fig. 5 Electrochemical results for various specimens in SBF: **a** potentiodynamic polarization curves; **b** Nyquist plots; **c** Bode plots of lg |*Z*| vs. frequency; **d** phase angles vs. frequency; **e** EEC for the specimens. SBF: simulated body fluid; EEC: equivalent electric circuit; R_s: the solution resistance; R_f: the oxide film resistance; CPE: constant phase element; R_{ct}: the charge transfer resistance

Table 1 Electrochemical parameters of the specimens in the SBF solution

Specimen	E_{corr} (V)	i_{corr} (mA)	MR (g/(m^2·d))	CR (mm/a)
βTi	−0.18	0.047	12.54	0.73
TiNT	−0.19	0.040	10.55	0.62
TiNTAg	−0.10	0.013	3.37	0.20
TiNTAg@HA	−0.09	0.011	2.87	0.17
TiNTAg@$CaSiO_3$	−0.10	0.017	4.45	0.26
TiNTAg@β-TCP	−0.09	0.001	0.26	0.02

SBF: simulated body fluid; MR: mass loss rate; CR: corrosion rate

Table 2 EIS fitting parameters of each specimen in the SBF solution

Specimen	R_s (Ω·cm^2)	R_f (Ω·cm^2)	CPE_1 (Ω^{-1}·cm^{-2}·s^n)	n_1	CPE_2 (Ω^{-1}·cm^{-2}·s^n)	n_2	R_{ct} (Ω·cm^2)
βTi	11.1	–	9.54×10^{-6}	0.75	–	–	2.17×10^{4}
TiNT	14.0	1.57×10^{5}	6.83×10^{-4}	0.026	7.01×10^{-5}	0.62	5.70×10^{4}
TiNTAg	20.3	6.93×10^{3}	9.89×10^{-6}	0.70	2.02×10^{-5}	0.68	7.35×10^{4}
TiNTAg@HA	20.8	4.72×10^{4}	1.30×10^{-5}	0.69	6.1×10^{-4}	0.32	4.80×10^{4}
TiNTAg@$CaSiO_3$	22.7	4.48×10^{3}	1.02×10^{-4}	0.11	9.71×10^{-5}	0.81	3.46×10^{4}
TiNTAg@β-TCP	10.3	4.54×10^{4}	1.61×10^{-4}	0.49	1.20×10^{-4}	0.76	7.73×10^{4}

EIS: electrochemical impedance spectroscopy; SBF: simulated body fluid

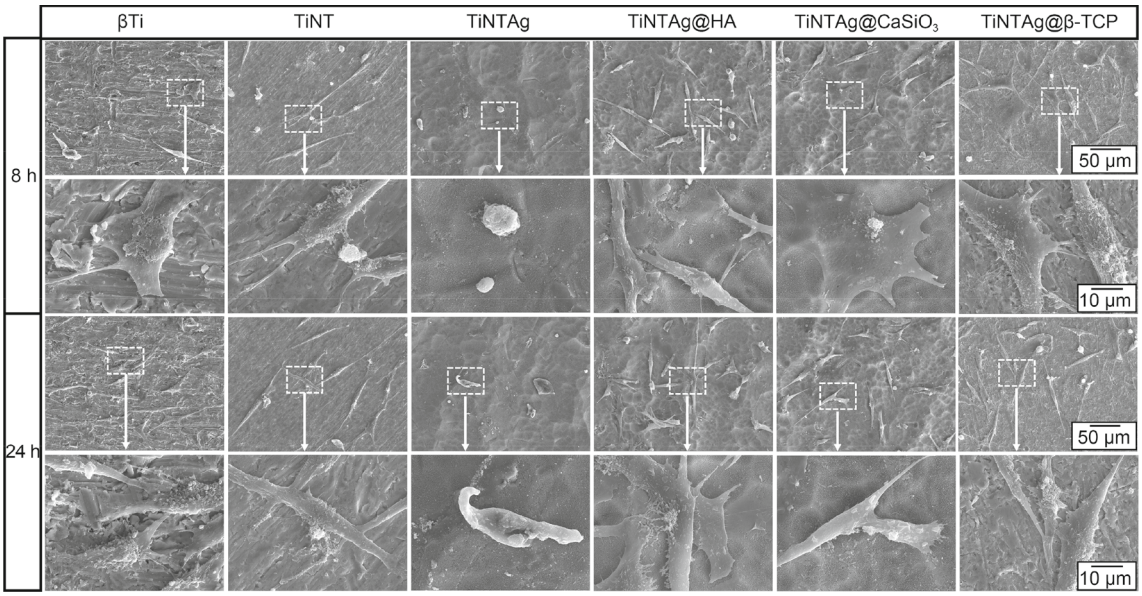

Fig. 6 SE images of MC3T3-E1 cells on the surface of the specimen after 8 and 24 h of incubation. SE: secondary electron

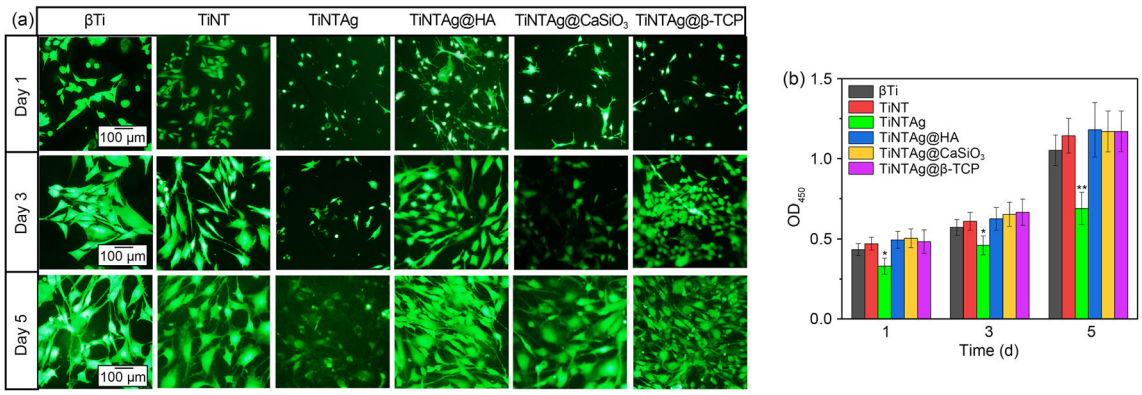

Fig. 7 Fluorescent staining images and viability of MC3T3-E1 cells in response to various surfaces after evaluation with **a** calcein–AM staining (scale bar: 100 μm) and **b** CCK-8 assay for 1, 3, and 5 days. Data are represented as mean±standard deviation ($n = 3$); $^{*}p<0.05$ and $^{**}p<0.01$ compared to βTi. OD_{450}: optical density at 450 nm; CCK: cell counting kit-8

Discussion

Wear behavior

Friction and wear are important factors in metal-to-bone contact during the osseointegration process. Tribocorrosion resistance depends on surface characteristics, especially surface coatings. Notably, COFs under purely mechanical wear are quite different from tribocorrosion. Some studies have reported that the COFs of Ti alloys were higher under conditions of tribocorrosion than under conditions of purely mechanical wear because the fluid environment accelerated wear loss [38, 41]; in particular, the coatings corroded, increasing frictional forces under tribocorrosion, which caused further wear loss [31]. In this study, the COFs under tribocorrosion conditions were higher than those under purely mechanical wear conditions (Fig. 3a) [31]. A similar phenomenon was observed in a study by Xu et al. [41], which showed that for Ti–16Mo and Ti–Mo–Cu, the COFs during tribocorrosion were higher than those obtained under dry wear conditions.

To further clarify the tribocorrosion mechanisms, we discuss the wear track surface morphologies. The wear tracks of the βTi showed irregular and deep plowing lines along the direction of the circle because the debris from the TNTZ alloy was embedded in the contact region and moved with the counterpart of GCr15 [42, 43] (see Figs. 4a and 4b). This can be attributed to the high hardness of the GCr15 ball. Severe plastic deformation was observed along the tracks due to the TNTZ debris. Based on this evidence, the wear mechanism

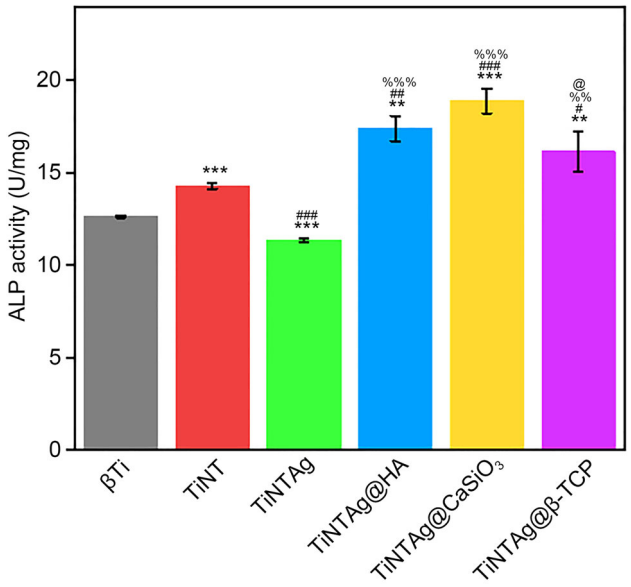

Fig. 8 ALP activity of MC3T3-E1 cells incubated for seven days. Data are represented as mean±standard deviation (n=3); $^{**}p$<0.01 and $^{***}p$<0.001 compared to βTi; $^{\#}p$<0.05, $^{\#\#}p$<0.01, and $^{\#\#\#}p$<0.001 compared to TiNT; $^{\%\%}p$<0.01 and $^{\%\%\%}p$<0.001 compared to TiNTAg; $^{@}p$<0.05 compared to TiNTAg@$CaSiO_3$. ALP: alkaline phosphatase

of the βTi involves abrasive wear during the tribocorrosion process.

As shown in Figs. 3 and 4, the TiNT exhibited shallower plowing lines and less debris than βTi. The TNTs were crushed between the TiO_2 debris and the TNTZ substrate, where the TiO_2 acted as the third-body wear debris (see Fig. 4m) [44]. The middle region in Fig. 4d shows that the main behavior was crushing TNTs and densification in the top zone, which resulted in delamination and even detachment of the TNTs and the generation of wear debris under a continuous tangential friction force and a normal load [45]. The wear debris was compressed to form a plastically deformed hardened coating that protected the substrate. The TiO_2 debris accelerated the abrasive wear and caused small scratches. The dynamic pressure lubrication effect decreased the normal pressure and improved the antiadhesive wear property. Moreover, the TNTs enhanced the hydrophilicity and held fluid at the interface. TNTs covered the substrate, which led to thicker lubrication, and turned the boundary lubrication into fluid lubrication. To summarize, the wear process of TiNT is demonstrated in Fig. 4m. The wear process can be divided into three phases, i.e., partial crushing, full densification, and failure.

The wear rates of TiNTAg@HA, TiNTAg@$CaSiO_3$, and TiNTAg@β-TCP showed remarkable differences. The reason for this was that both HA and β-TCP particles contained dispersed nano- and microparticles, whereas the $CaSiO_3$ powder was inhomogeneous and consisted of large agglomerated particles. After HA, $CaSiO_3$, and β-TCP particles coated Ag NPs, different particle sizes showed the difference of wear processes. In TiNTAg@HA, the HA particles protected the TNTs as a barrier from the shear force generated by the pressure and lateral friction and delayed the damage to the nanotubes. Meanwhile, the microbar rolled at the interface of the counterpart, and the TNTs produced a slight plow, which resulted in the lowest wear rate (Figs. 4g and 4h). However, the β-TCP particle debris could not be pressed into the nanotubes, and instead, it stuck to the GCr15

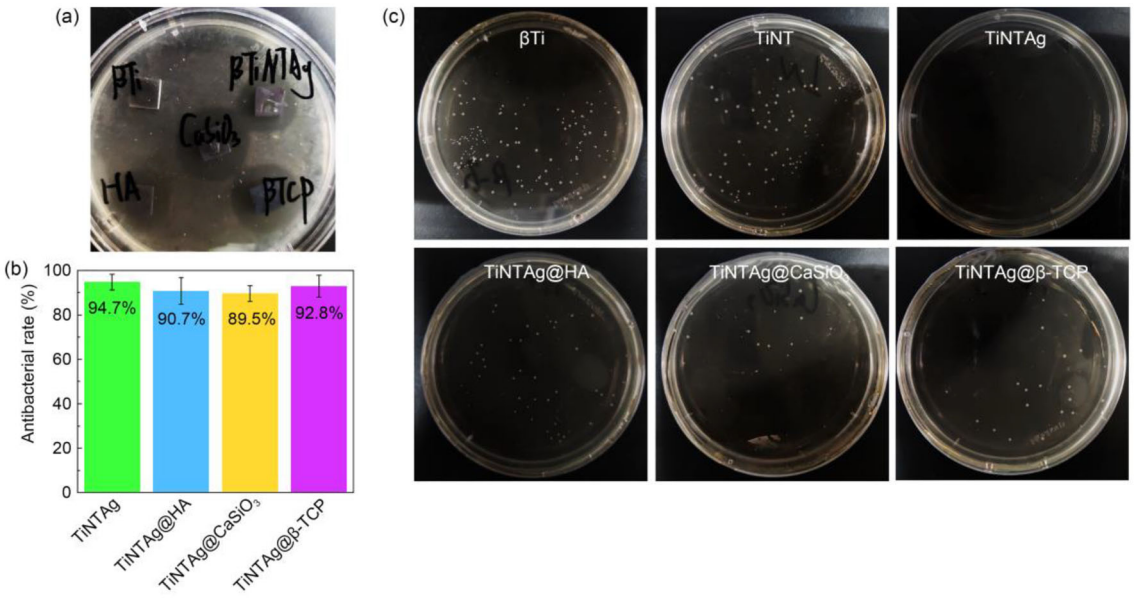

Fig. 9 **a** Inhibition ring experiment against *E. coli* after 12 h incubation of each group; **b** inhibition rates against *E. coli*; **c** *E. coli* colonies on agar plates after 12-h incubation of each group. *E. coli*: *Escherichia coli*

ball, which prevented the counterpart from moving. This led to deep plowing in the wear tracks (Figs. 4k and 4l). The $CaSiO_3$ particles accelerated the destruction of the TNTs because of their large size (Figs. 4i and 4j). In the final stage of the wear process, all three specimens underwent partial densification, total densification at the top of the nanotubes, and then failure. Eventually, the substrate was exposed, and the counterpart contacted the substrate.

Corrosion behavior

The corrosion behavior mainly depends on the passive films being able to delay liquid penetration into the substrate [46]. The passive films on the surface of titanium alloys are affected by changes in pH and surface wear. Toxic ions can be released into the regions that surround implants, and these ultimately end up in the blood, urine, and organs, which may impact cell function and provoke an immune response. To endow TNTZ with better corrosion resistance, specific coatings can be applied to the surface as a barrier to reduce its CR. In this study, the coatings brought about remarkable improvements to the CR of the substrate. Hence, it is of great interest to clarify how the β-TCP particle-doped TNTs improve their corrosion behavior when they are subjected to SBF.

In general, two main factors can improve the functionality of passive films, including the thickness of the films and their structure [17]. The electrochemical behavior of the specimens was investigated in SBF (Fig. 5). Although an oxide film formed on the TNTZ substrate, it was thin and loose and had difficulty in inhibiting corrosion. R_{ct} reflects the ease that the charge transition goes through the interface between the electrode and the electrolyte solution. In contrast, the R_{ct} values of all the modified composites were higher than those of the substrate (Table 2).

The incorporation of particles decreased the corrosion current density of the anodic polarization curve by several orders of magnitude (Table 1). Mazare et al. [47] found that the corrosion resistance of TNTs improved with increasing annealing temperature (from 350 to 750 °C), leading to the rutile contents increasing from 15% to 95%. In another study, it was demonstrated that the corrosion protection offered by TNT coating decreased with increasing anodization voltage (from 10 to 50 V) [48]. In this study, the TNTs have outer tube films and inner barrier films. Hence, the EEC of the TiNT can be described using $R_s(CPE_1R_f)(CPE_2R_{ct})$, where CPE_2 and R_f represent the TNT film and oxide film resistance at high frequencies, respectively. CPE_1 and R_{ct} reflect the double-layer capacitance and charge transfer resistance at low frequencies [39]. Hence, TNTs show better corrosion resistance than βTi, which is in agreement with the findings of other studies [47, 49].

Notably, a passivation zone appeared at an i_{corr} of 1×10^{-6} A/cm^2 for TiNTAg@β-TCP, which corresponded to a higher |*Z*| and a higher phase angle (see Fig. 5). The passive region extended over a wide potential range, which suggested the rapid passivation behavior of TiNTAg@β-TCP. This phenomenon primarily depends on the fast blockage of the current supplied by the β-TCP particles. The equivalent circuit for the β-TCP nanocomposite can be described using $R_s(CPE_1R_f)(CPE_2R_{ct})$, which is in agreement with an earlier study on Ca/P-doped TNTs [25]. In particular, the circuit required that a higher charge be involved in the process to provide better corrosion resistance. The good corrosion resistance of TiNTAg@β-TCP could be attributed to three factors. First, the compact coating with a combination of TNTs and β-TCP restricted the movement of metal ions from the metallic surface to the surrounding solution, which provided a high physical barrier. Second, β-TCP induced the depositions of Ca and P products on the implants. The products covered the coating, thickened the barrier, and delayed the corrosion behavior of the substrate. Third, the NPs and TNTs provided a twisty route, thereby producing a maze effect. The maze effect increased the distance between the matrix and the corrosion solution, delaying the corrosion behavior.

Cell response

As is well known, cell behavior depends on surface features and chemical composition of coatings [23]. Osteoblast adhesion is the first step in material surface interactions and affects cell proliferation and ALP activity.

Generally, high cytotoxicity can be attributed to metal ion release. It was found that TNTZ, TNTs, Ag NPs, and β-TCP present no detectable cytotoxicity to bone marrow mesenchymal stem cells (BMSCs) [31]. Cytotoxicity due to Ag ion can be prevented using a slow release layer and keeping the Ag^+ concentration (HA: 0.54 mg/L; $CaSiO_3$: 0.33 mg/L; β-TCP: 0.61 mg/L) below the concentration threshold of 0.66 mg/L [50]. In particular, the Ca^{2+} and anions released from the specimen surface had great effects on the proliferation of the MC3T3-E1 cells. More MC3T3-E1 cells adhered to the surfaces of TiNTAg@HA, TiNTAg@$CaSiO_3$, and TiNTAg@β-TCP than TiNTAg after early-incubation (8 and 24 h) and mid-incubation (1, 3, and 5 days) periods. These studies are in good agreement with other studies [51–53].

ALP activity in osteoblasts is an early biochemical indicator of osteogenesis [26, 54, 55]. High levels of ALP activity can induce the initial mineralization and further growth of hydroxyapatite crystals [56]. In this study, Si-loaded coatings displayed more positive ALP activity than TiNTAg@$CaSiO_3$. This effect may have been caused by the release of SiO_3^{2-} from TiNTAg@$CaSiO_3$, which plays a role in the growth factor of MC3T3-E1 cells. Thus, the presence of Si was favorable to the MC3T3-E1 cells during early growth [33]. Ando et al. [57] showed that the incorporation of Si into calcium phosphate had a positive effect on

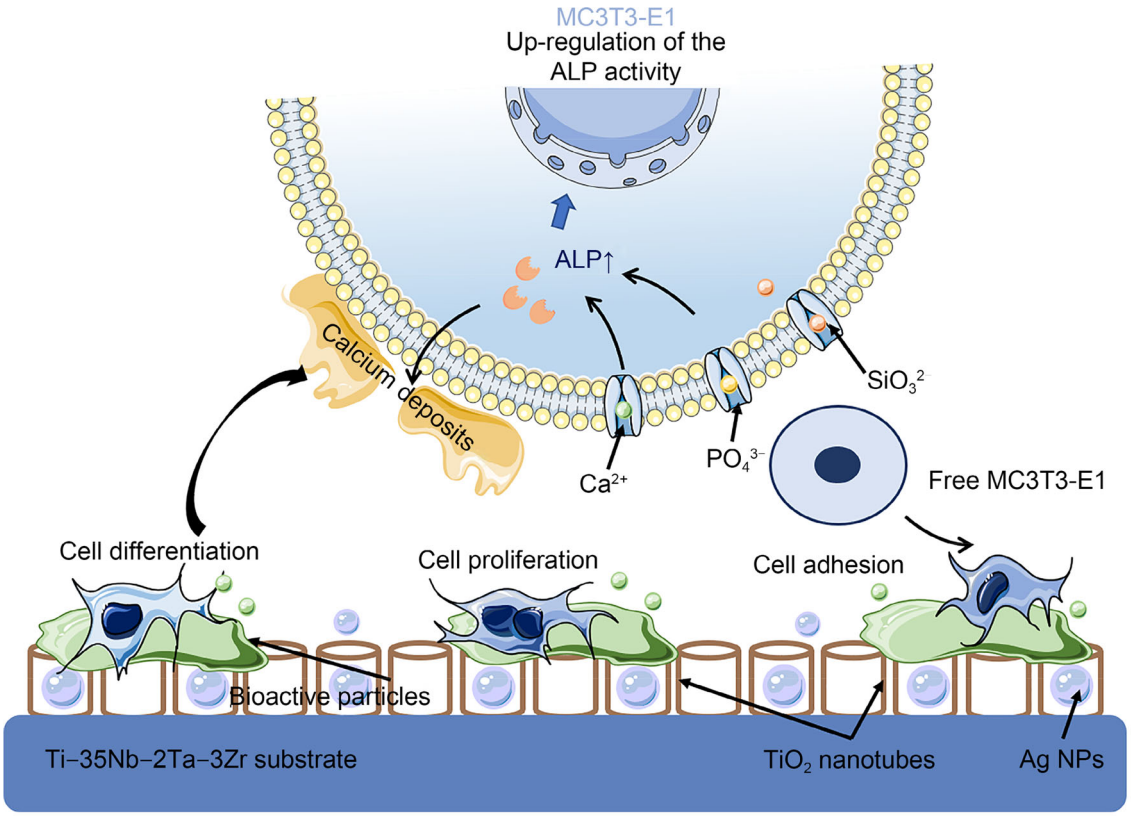

Fig. 10 Schematic of MC3T3-E1 cell growth on the specimen. ALP: alkaline phosphatase; NPs: nanoparticles

osteoblast proliferation and on the expression of transforming growth factor-β (TGF-β) mRNA in human osteoblasts. In another study [58], $CaSiO_3$ promoted osteogenesis. Moreover, Si induced osteoblast proliferation and the formation of the bone extracellular matrix [32]. In the present study, the cell growth encountered no cytotoxicity and showed good osteogenic performance on the $CaSiO_3$ surface. The incorporation of $CaSiO_3$ into TNTs can transform their surface characteristics, which leads to the up-regulated expression of osteogenic genes and improves cell adhesion, proliferation, and differentiation [52]. Figure 10 shows a schematic of the interaction between the MC3T3-E1 cell and the bioceramics. After it comes into contact with the coating surface, the MC3T3-E1 cell with a spindle shape and good outstretched filopodia spreads to a larger area. The Ca^{2+} and anions, including PO_4^{3-} and SiO_3^{2-}, were released from the particles. These ions entered cells through cell membrane channels, causing an up-regulation of the ALP activity.

As noted earlier, osteogenic behavior depends on surface feature and chemical composition of the implant, which play a key role in promoting cell response and enhancing interactions between the bone and the implant. Surface features, such as micro-HA, meso-$CaSiO_3$, and nano-β-TCP particles, and the released mineral ions from the hybrid coatings, such as SiO_3^{2-} and PO_4^{3-}, promote ALP activity.

Conclusions

In this study, TNTs were coated with Ag NPs and bioceramics (nano-β-TCP, micro-HA, and meso-$CaSiO_3$) using anodization, deposition, and spin-coating methods. Their effects on the wear, corrosion resistance, and bioactivity of multiscale structures were studied. The conclusions of this study are as follows:

(1) The micro-HA ((50.2±15.4) μm) coating on the TNTs produced substantial tribocorrosion resistance (wear rate: 1.26×10^{-3} $mm^3/(N\cdot m)$), where the wear mechanism was a combination of adhesive and abrasive wear (including third-body abrasion).
(2) The nano-β-TCP ((310±90) nm) coating exhibited excellent corrosion resistance with a low CR of 0.02 mm/a because of the physical barrier, deposition, and maze effect.
(3) The incorporation of Si and P improved adhesion and proliferation as well as the ALP activity of the MC3T3-E1 cells. Within the safety threshold (0.66 mg/L), Ag^+ endowed the coatings with antibacterial properties and exhibited an antibacterial rate of ≥89.5%.

Hence, these multiscale coatings containing ceramics are a promising method for controlling surface structure and composition as well as for improving wear resistance and corrosion resistance.

Supplementary Information The online version contains supplementary material available at https://doi.org/10.1007/s42242-024-00279-1.

Acknowledgements This work was supported by the National Natural Science Foundation of China (Nos. 52071346, 52111530193, and 52274387), the Natural Science Foundation of Hunan Province for Distinguished Young Scholars (No. 2023JJ10075), the Hunan Provincial Natural Science Foundation of China (No. 2021JJ30846), the Central South University Research Program of Advanced Interdisciplinary Studies (No. 2023QYJC038), the Funding for the Medical Engineering Cross Disciplinary Project at Shanghai Jiao Tong University, and the Fundamental Research Funds for the Central Universities of Central South University (No. 2022ZZTS0402). The authors would also thank Sinoma Institute of Materials Research (Guangzhou) Co., Ltd. for the assistance with the TEM characterization.

Author contributions QGW was responsible for resources, conceptualization, and writing—original draft. JL and CLY carried out formal analysis, data curation, and validation. JBL and VVU conducted investigation. HW and LQW were involved in supervision, funding acquisition, and validation. XXY and SFL assisted with methodology. YJR, LXL, and IB contributed to writing—review and editing.

Declarations

Conflict of interest The authors declare that they have no conflict of interest.

Ethical approval This article does not contain any studies with human or animal subjects performed by any of the authors.

References

1. Guo LY, Naghavi SA, Wang ZQ et al (2022) On the design evolution of hip implants: a review. Mater Des 216:110552. https://doi.org/10.1016/j.matdes.2022.110552
2. Wang MC, Bu FX, Zhou CJ et al (2020) Bonding performance and mechanism of a heat-resistant composite precursor adhesive (RT-1000C) for TC4 titanium alloy. J Micromech Mol Phys 5(4):2050016. https://doi.org/10.1142/S2424913020500162
3. Zhang TL, Liu CT (2022) Design of titanium alloys by additive manufacturing: a critical review. Adv Powder Mater 1(1):100014. https://doi.org/10.1016/j.apmate.2021.11.001
4. Li XZ, Huang QL, Liu L et al (2018) Reduced inflammatory response by incorporating magnesium into porous TiO_2 coating on titanium substrate. Colloid Surf B Biointerfaces 171:276–284. https://doi.org/10.1016/j.colsurfb.2018.07.032
5. Lan XD, Wu H, Liu Y et al (2016) Microstructures and tribological properties of laser cladded Ti-based metallic glass composite coatings. Mater Charact 120:82–89. https://doi.org/10.1016/j.matchar.2016.08.026
6. Cai DG, Zhao XT, Yang L et al (2021) A novel biomedical titanium alloy with high antibacterial property and low elastic modulus. J Mater Sci Technol 81:13–25. https://doi.org/10.1016/j.jmst.2021.01.015
7. Wang JC, Liu YJ, Liang SX et al (2022) Comparison of microstructure and mechanical behavior of Ti-35Nb manufactured by laser powder bed fusion from elemental powder mixture and prealloyed powder. J Mater Sci Technol 105:1–16. https://doi.org/10.1016/j.jmst.2021.07.021
8. Hu J, Ren YJ, Huang QL et al (2021) Microstructure and corrosion behavior of Ti-Nb coatings on NiTi substrate fabricated by laser cladding. Coatings 11(5):597. https://doi.org/10.3390/coatings11050597
9. Chen ZJ, Liu Y, Wu H et al (2015) Microstructures and wear properties of surface treated Ti–36Nb–2Ta–3Zr–0.35O alloy by electron beam melting (EBM). Appl Surf Sci 357:2347–2354. https://doi.org/10.1016/j.apsusc.2015.09.240
10. Zhang T, Wei DX, Lu EY et al (2022) Microstructure evolution and deformation mechanism of α+β dual-phase Ti-*x*Nb-*y*Ta-2Zr alloys with high performance. J Mater Sci Technol 131:68–81. https://doi.org/10.1016/j.jmst.2022.04.052
11. Ren YJ, Han B, Wu H et al (2022) Copper segregation-mediated formation of nanotwins and 9R phases in titanium alloy produced by laser powder bed fusion. Scripta Mater 224:115115. https://doi.org/10.1016/j.scriptamat.2022.115115
12. Guo YY, Chen DS, Lu WJ et al (2013) Corrosion resistance and in vitro response of a novel Ti35Nb2Ta3Zr alloy with a low Young's modulus. Biomed Mater 8(5):055004. https://doi.org/10.1088/1748-6041/8/5/055004
13. Shao LF, Du YH, Dai K et al (2021) β-Ti alloys for orthopedic and dental applications: a review of progress on improvement of properties through surface modification. Coatings 11(12):1446. https://doi.org/10.3390/coatings11121446
14. Feng JY, Wei DX, Zhang PL et al (2023) Preparation of TiNbTaZrMo high-entropy alloy with tunable Young's modulus by selective laser melting. J Manuf Process 85:160–165. https://doi.org/10.1016/j.jmapro.2022.11.046
15. Mao CY, Yu WJ, Jin M et al (2022) Mechanobiologically optimized Ti-35Nb-2Ta-3Zr improves load transduction and enhances bone remodeling in tilted dental implant therapy. Bioact Mater 16:15–26. https://doi.org/10.1016/j.bioactmat.2022.03.005
16. Fang YJ, Wang QG, Yang Z et al (2022) An efficient approach to endow TiNbTaZr implant with osteogenic differentiation and antibacterial activity in vitro. Mater Des 221:110987. https://doi.org/10.1016/j.matdes.2022.110987
17. Gu H, Ding ZH, Yang Z et al (2019) Microstructure evolution and electrochemical properties of TiO_2/Ti-35Nb-2Ta-3Zr micro/nano-composites fabricated by friction stir processing. Mater Des 169:107680. https://doi.org/10.1016/j.matdes.2019.107680
18. Huang QL, Li XZ, Liu T et al (2018) Enhanced SaOS-2 cell adhesion, proliferation and differentiation on Mg-incorporated micro/nano-topographical TiO_2 coatings. Appl Surf Sci 447:767–776. https://doi.org/10.1016/j.apsusc.2018.04.095
19. Liu WT, Liang LX, Liu B et al (2021) The response of macrophages and their osteogenic potential modulated by micro/nano-structured Ti surfaces. Colloid Surf B Biointerfaces 205:111848. https://doi.org/10.1016/j.colsurfb.2021.111848
20. Li XZ, Huang QL, Elkhooly TA et al (2018) Effects of titanium surface roughness on the mediation of osteogenesis via modulating the immune response of macrophages. Biomed Mater 13(4):045013. https://doi.org/10.1088/1748-605X/aabe33
21. Huang QL, Li XZ, Elkhooly TA et al (2018) The osteogenic, inflammatory and osteo-immunomodulatory performances of biomedical Ti-Ta metal–metal composite with Ca- and Si-containing bioceramic coatings. Colloid Surf B Biointerfaces 169:49–59. https://doi.org/10.1016/j.colsurfb.2018.05.010
22. Huang QL, Li XZ, Elkhooly TA et al (2018) The Cu-containing TiO_2 coatings with modulatory effects on macrophage polarization and bactericidal capacity prepared by micro-arc oxidation on titanium substrates. Colloid Surf B Biointerfaces 170:242–250. https://doi.org/10.1016/j.colsurfb.2018.06.020

23. Wang QG, Zhou P, Liu SF et al (2020) Multi-scale surface treatments of titanium implants for rapid osseointegration: a review. Nanomaterials 10(6):1244. https://doi.org/10.3390/nano10061244
24. Yu WQ, Qian C, Jiang XQ et al (2015) Mechanisms of stem cell osteogenic differentiation on TiO_2 nanotubes. Colloid Surf B Biointerfaces 136:779–785. https://doi.org/10.1016/j.colsurfb.2015.10.019
25. Alves SA, Patel SB, Sukotjo C et al (2017) Synthesis of calcium-phosphorous doped TiO_2 nanotubes by anodization and reverse polarization: a promising strategy for an efficient biofunctional implant surface. Appl Surf Sci 399:682–701. https://doi.org/10.1016/j.apsusc.2016.12.105
26. Zhang YN, Wang K, Song Y et al (2020) Ca substitution of Sr in Sr-doped TiO_2 nanotube film on Ti surface for enhanced osteogenic activity. Appl Surf Sci 528:147055. https://doi.org/10.1016/j.apsusc.2020.147055
27. Shen K, Tang Q, Fang XT et al (2020) The sustained release of dexamethasone from TiO_2 nanotubes reinforced by chitosan to enhance osteoblast function and anti-inflammation activity. Mater Sci Eng C Mater Biol Appl 116:111241. https://doi.org/10.1016/j.msec.2020.111241
28. Ferraris S, Spriano S (2016) Antibacterial titanium surfaces for medical implants. Mater Sci Eng C Mater Biol Appl 61:965–978. https://doi.org/10.1016/j.msec.2015.12.062
29. Yang Z, Gu H, Sha G et al (2018) TC4/Ag metal matrix nanocomposites modified by friction stir processing: surface characterization, antibacterial property, and cytotoxicity in vitro. ACS Appl Mater Interfaces 10(48):41155–41166. https://doi.org/10.1021/acsami.8b16343
30. Mei SL, Wang HY, Wang W et al (2014) Antibacterial effects and biocompatibility of titanium surfaces with graded silver incorporation in titania nanotubes. Biomaterials 35(14):4255–4265. https://doi.org/10.1016/j.biomaterials.2014.02.005
31. Liu SF, Wang QG, Liu W et al (2021) Multi-scale hybrid modified coatings on titanium implants for non-cytotoxicity and antibacterial properties. Nanoscale 13(23):10587–10599. https://doi.org/10.1039/d1nr02459k
32. Huang Y, Xu ZW, Zhang XJ et al (2017) Nanotube-formed Ti substrates coated with silicate/silver co-doped hydroxyapatite as prospective materials for bone implants. J Alloy Compd 697:182–199. https://doi.org/10.1016/j.jallcom.2016.12.139
33. Huang Y, Han SG, Pang XF et al (2013) Electrodeposition of porous hydroxyapatite/calcium silicate composite coating on titanium for biomedical applications. Appl Surf Sci 271:299–302. https://doi.org/10.1016/j.apsusc.2013.01.187
34. Samanta SK, Devi KB, Das P et al (2019) Metallic ion doped tricalcium phosphate ceramics: effect of dynamic loading on in vivo bone regeneration. J Mech Behav Biomed Mater 96:227–235. https://doi.org/10.1016/j.jmbbm.2019.04.051
35. Schmidt-Stein F, Thiemann S, Berger S et al (2010) Mechanical properties of anatase and semi-metallic TiO_2 nanotubes. Acta Mater 58(19):6317–6323. https://doi.org/10.1016/j.actamat.2010.07.053
36. Ha Y, Yang J, Tao F et al (2018) Phase-transited lysozyme as a universal route to bioactive hydroxyapatite crystalline film. Adv Funct Mater 28(4):1704476. https://doi.org/10.1002/adfm.201704476
37. Sanosh KP, Chu MC, Balakrishnan A et al (2010) Sol–gel synthesis of pure nano sized β-tricalcium phosphate crystalline powders. Curr Appl Phys 10(1):68–71. https://doi.org/10.1016/j.cap.2009.04.014
38. Lu X, Zhang DW, Xu W et al (2020) The effect of Cu content on corrosion, wear and tribocorrosion resistance of Ti-Mo-Cu alloy for load-bearing bone implants. Corros Sci 177:109007. https://doi.org/10.1016/j.corsci.2020.109007
39. Cui SW, Yin XY, Yu QL et al (2015) Polypyrrole nanowire/TiO_2 nanotube nanocomposites as photoanodes for photocathodic protection of Ti substrate and 304 stainless steel under visible light. Corros Sci 98:471–477. https://doi.org/10.1016/j.corsci.2015.05.059
40. Carlson C, Hussain SM, Schrand AM et al (2008) Unique cellular interaction of silver nanoparticles: size-dependent generation of reactive oxygen species. J Phys Chem B 112(43):13608–13619. https://doi.org/10.1021/jp712087m
41. Xu W, Yu AH, Lu X et al (2020) Synergistic interactions between wear and corrosion of Ti-16Mo orthopedic alloy. J Mater Res Technol 9(5):9996–10003. https://doi.org/10.1016/j.jmrt.2020.06.095
42. Alves SA, Rossi AL, Ribeiro AR et al (2017) Tribo-electrochemical behavior of bio-functionalized TiO_2 nanotubes in artificial saliva: understanding of degradation mechanisms. Wear 384–385:28–42. https://doi.org/10.1016/j.wear.2017.05.005
43. Chan CW, Lee S, Smith G et al (2016) Enhancement of wear and corrosion resistance of beta titanium alloy by laser gas alloying with nitrogen. Appl Surf Sci 367:80–90. https://doi.org/10.1016/j.apsusc.2016.01.091
44. Wang HD, He PF, Ma GZ et al (2018) Tribological behavior of plasma sprayed carbon nanotubes reinforced TiO_2 coatings. J Eur Ceram Soc 38(10):3660–3672. https://doi.org/10.1016/j.jeurceramsoc.2018.04.019
45. Wang GQ, Wang SR, Yang XF et al (2021) Fretting wear and mechanical properties of surface-nanostructural titanium alloy bone plate. Surf Coat Tech 405:126512. https://doi.org/10.1016/j.surfcoat.2020.126512
46. Cui YW, Chen LY, Chu YH et al (2023) Metastable pitting corrosion behavior and characteristics of passive film of laser powder bed fusion produced Ti–6Al–4V in NaCl solutions with different concentrations. Corros Sci 215:111017. https://doi.org/10.1016/j.corsci.2023.111017
47. Mazare A, Totea G, Burnei C et al (2016) Corrosion, antibacterial activity and haemocompatibility of TiO_2 nanotubes as a function of their annealing temperature. Corros Sci 103:215–222. https://doi.org/10.1016/j.corsci.2015.11.021
48. Çırak BB, Karadeniz SM, Kılınç T et al (2017) Synthesis, surface properties, crystal structure and dye sensitized solar cell performance of TiO_2 nanotube arrays anodized under different voltages. Vacuum 144:183–189. https://doi.org/10.1016/j.vacuum.2017.07.037
49. Wu SX, Wang SR, Liu WT et al (2019) Microstructure and properties of TiO_2 nanotube coatings on bone plate surface fabrication by anodic oxidation. Surf Coat Tech 374:362–373. https://doi.org/10.1016/j.surfcoat.2019.06.019
50. Foldbjerg R, Olesen P, Hougaard M et al (2009) PVP-coated silver nanoparticles and silver ions induce reactive oxygen species, apoptosis and necrosis in THP-1 monocytes. Toxicol Lett 190(2):156–162. https://doi.org/10.1016/j.toxlet.2009.07.009
51. Siek D, Ślósarczyk A, Przekora A et al (2017) Evaluation of antibacterial activity and cytocompatibility of α-TCP based bone cements with silver-doped hydroxyapatite and $CaCO_3$. Ceram Int 43(16):13997–14007. https://doi.org/10.1016/j.ceramint.2017.07.131
52. Lee DK, Ki MR, Kim EH et al (2021) Biosilicated collagen/beta-tricalcium phosphate composites as a BMP-2-delivering bone-graft substitute for accelerated craniofacial bone regeneration. Biomater Res 25(1):2–11. https://doi.org/10.1186/s40824-021-00214-w
53. Yu JM, Li K, Zheng XB et al (2013) In vitro and in vivo evaluation of zinc-modified Ca-Si-based ceramic coating for bone implants. PLoS ONE 8(3):e57564. https://doi.org/10.1371/journal.pone.0057564
54. Liang LX, Huang QL, Wu H et al (2022) Engineering nanostructures with controllable dimensional features on micro-topographical titanium surfaces to modulate the activation degree

of M1 macrophages and their osteogenic potential. J Mater Sci Technol 96:167–178. https://doi.org/10.1016/j.jmst.2021.03.078
55. Liang LX, Huang QL, Wu H et al (2021) Stimulation of in vitro and in vivo osteogenesis by Ti-Mg alloys with the sustained-release function of magnesium ions. Colloid Surf B Biointerfaces 197:111360. https://doi.org/10.1016/j.colsurfb.2020.111360
56. Kang MH, Lee SJ, Lee MH (2020) Bone remodeling effects of Korean Red Ginseng extracts for dental implant applications. J Ginseng Res 44(6):823–832. https://doi.org/10.1016/j.jgr.2020.05.003
57. Ando Y, Miyamoto H, Noda I et al (2010) Calcium phosphate coating containing silver shows high antibacterial activity and low cytotoxicity and inhibits bacterial adhesion. Mater Sci Eng C Mater Biol Appl 30(1):175–180. https://doi.org/10.1016/j.msec.2009.09.015
58. Xue WC, Liu XY, Zheng XB et al (2005) In vivo evaluation of plasma-sprayed wollastonite coating. Biomaterials 26(17):3455–3460. https://doi.org/10.1016/j.biomaterials.2004.09.027